scientific reports

Check for updates

OPEN

Effect of Mn content on the corrosion behavior and biocompatibility of biodegradable Zn-Mn alloys

Xin Cheng[1], Qiuju Lin[1], Hongxi Jin[2], Fufang Han[2], Xiaohui Dou[2], Xinwei Zhang[2], Zonghao He[2], Chuan He[2], Songnan Zhao[2] & Dalei Zhang[2]✉

Zinc-based alloys have attracted increasing attention as biodegradable metals by virtue of their excellent mechanical, degradable and biocompatible properties. By introducing different levels of manganese (0.1, 0.3, 0.5 and 0.8 *wt*%), the properties of pure zinc were improved. The obtained zinc-manganese alloys consisted mainly of a zinc matrix and a $MnZn_{13}$ phase, which led to a significant improvement of the mechanical properties with ultimate tensile strength (UTS), yield strength (YS) and elongation up to 117.3 MPa, 110.4 MPa, and 14%, respectively, and a Vickers hardness of 78 HV. After immersion in simulated body fluid (SBF), the addition of manganese slightly slowed down the corrosion rate of pure zinc, with an average corrosion rate of approximately 0.12 mm/y. Subsequent electrochemical tests and scanning Kelvin probe tests further confirmed this observation. In addition, the zinc-manganese alloys showed better resistance to E. coli and Staphylococcus aureus than pure zinc according to antimicrobial and in vitro cytotoxicity tests. Cell viability in the alloy extraction solution was higher than that of pure zinc and remained within acceptable limits (> 75%). In summary, Zn-Mn alloy has excellent performance, the promoting effect of Mn element on osteogenesis, and the excellent mechanical properties of the alloy itself, making it a potential biodegradable material for orthopedics.

Keywords Zn-Mn alloy, Biodegradable alloy, $MnZn_{13}$, Mechanical properties, Biocompatibility

In recent years, biodegradable alloy materials have received more and more attention owing to their advantages, such as good degradability and biocompatibility, which present a broad development prospect[1,2]. Previously, the main research focus was on magnesium and iron alloys, both of which have made significant progress[3–7]. However, iron alloys degrade too slowly[8,9], and they possess some magnetic properties that may interfere with postoperative examinations. On the other hand, magnesium alloys are subject to excessive degradation[10–12], and the released H_2 from the implantation site can lead to hydrogen accumulation[13,14], limiting their clinical application[7].

Zinc is one of the essential trace elements and is widely distributed in cells, with an adult needing to consume approximately 15 mg of zinc per day, and it plays a crucial role in cell signaling and in the synthesis of enzymes and proteins[15,16]. Therefore, it is indispensable in DNA replication and protein modification[17]. In addition, pure zinc has an electrode potential between magnesium and iron and a moderate corrosion rate, a property that makes it well suited to meet the mechanical and degradation performance requirements of implantable devices[18]. As a medical implant material, whether used for orthopaedic implants or cardiovascular stents, its degradation rate is a key performance indicator, and it is crucial to match the degradation rate to the therapeutic needs of the patient's condition, which will be the focus of future research.

However, the poor mechanical properties of pure zinc make it difficult to be used as a medical implant material[19]. Therefore, researchers have used alloying and rolling processes to improve the basic mechanical properties of zinc[20,21]. Currently, various elements such as Mn, Mg, Cu, Fe, Ca and Li are extensively added to zinc to form alloys, including Zn-Cu-Fe[22], Zn-Cu[23], Zn-Mn-Mg[24], Zn-Mn[25], Zn-Mg-Ca[26] and Zn-Li[27], etc. Such alloy compositions usually have good strength, but over time their mechanical properties degrade to unacceptable levels, a difficult problem that needs to be solved. Recent research results have shown that adding

[1]Qingdao Central Hospital, University of Health and Rehabilitation Sciences (Qingdao Central Hospital), Qingdao 266042, China. [2]School of Materials Science and Engineering, China University of Petroleum (East China), Qingdao 266580, China. ✉email: zhangdal2008@126.com

Mn[28] and Mg[29,30] elements to alloys has a certain impact on their mechanical properties and biocompatibility. The addition of these alloying elements also provides more possibilities for the study of biodegradable alloys.

A recent study has shown that the addition of manganese improves the elongation of zinc alloys[31]. In addition, manganese is one of the essential trace elements and plays an important role in activating various enzymes and is closely related to the synthesis of sugars and proteins in the body[32,33]. According to the phase diagram of Zn-Mn alloy, the second phase in Zn-Mn alloy is $MnZn_{13}$[25]. During hot extrusion, the combined effect of grain refinement and second phase precipitation leads to dynamic recrystallisation of the grains, which removes stresses within the alloy and confers good ductility[34]. In terms of biocompatibility, it has been shown that Zn-Mn alloys have good cytocompatibility and osteogenic activity[35], and thus are expected to be excellent biodegradable implantable materials in the future.

This study prepared Zn-(0.1, 0.3, 0.5, and 0.8 *wt*%) Mn alloys with different Mn contents using the melting method. The effect of added Mn on the mechanical properties and corrosion resistance of the alloys, especially the corrosion behavior before and after immersion in simulated body fluids, was systematically evaluated. In addition, the biocompatibility of the alloys was further investigated to ensure their potential as biodegradable materials. Finally, based on the experimental results, the effect of manganese addition on various properties of Zn-Mn alloys was analyzed and discussed in detail.

Materials and methods

Materials preparation

The metallic materials used in this study were pure Zn (99.995 *wt*%) and pure Mn (99.99 *wt*%) for the preparation of cast Zn-xMn (x = 0.1, 0.3, 0.5 and 0.8 *wt*%) alloys. Put the alloy material into the furnace and start heating when the internal pressure reaches 0.05 MPa under the protection of Ar gas atmosphere. After increasing the temperature to 745 °C and holding for 5 min, the molten alloy was cast into graphite moulds and then air-cooled. The actual chemical composition of the casting alloy was determined by Inductively Coupled Plasma Atomic Emission Spectroscopy (ICP-AES, Agilent 725-ES, USA), and the results are shown in Table 1. Homogenize the as cast alloy after determining its composition, and place the raw material at 260 ℃ for 2–3 h before cooling it in the furnace to eliminate residual stresses generated during processing. Subsequently, the alloy was cut into cylindrical specimens with a diameter of 10 mm and a height of 5 mm using an electric discharge numerical control wire cutting machine. The cut specimens were polished with SiC papers of 240#, 600#, 1000#, 1500# and 2000#, followed by ultrasonically cleaned with deionized water and anhydrous ethanol, and then air-dried.

Microstructure characterization and phase analysis

The polished specimens were further polished with diamond polishing paste and etched with acid solution (4% nitric acid in ethanol). Subsequently, the microstructure and elemental composition of the materials were analyzed using an optical microscope (OM, Zeiss Axio Observer A1, Germany) and a scanning electron microscope (SEM, Hitachi Regulus SU8230, Japan) equipped with energy-dispersive X-ray spectroscopy (EDS, IXRF Model 550i, USA). Finally, the samples were physically analyzed using X-ray diffraction (XRD, D8 Advance, Germany) with CuKα targets in a scanning angle range of 10°-90° and a scanning speed of 10°/min.

Mechanical test

The hardness of the materials was measured using a Vickers hardness tester (Wilson VH3300, USA) by applying a load of 100 N for 10 s at five randomly selected points on each specimen. The tensile specimens were prepared according to GB/T228.1-2021 as shown in Fig. 1. Room temperature tensile tests were carried out on a universal testing machine (Instron 5969, USA) with a crosshead speed of 1 mm/min.

Antibacterial testing

To evaluate the antibacterial properties of the material, Escherichia coli and Staphylococcus aureus were prepared. The materials were first ground, then ultrasonically cleaned with ethanol, and subjected to high-temperature and high-pressure steam sterilization at 121 ℃ for 20 min. The E. coli and S. aureus suspensions were diluted with aseptic PBS solution to 10^6 CFU/mL. Subsequently, 100 µL of each bacterial suspension was evenly spread on LB solid culture medium. The sterilized samples were then placed on the surface of the culture medium, and the Petri dishes were incubated in a constant-temperature incubator at 37 ℃ for 24 h. At the end of the incubation, photographs were taken and the size of the zone of inhibition was measured.

In vitro cytotoxicity test

The cytotoxicity experiments were conducted according to ISO 10993-5:2009 standard. DMEM medium containing 10% fetal bovine serum and 1% penicillin-streptomycin was used, and the ratio of the surface area of the sample material to the volume of the extraction solution was 1.25 cm^2:1 mL. Cell viability was assessed

Alloy	Mn	Zn
Zn-0.1Mn	0.094	Bal.
Zn-0.3Mn	0.319	Bal.
Zn-0.5Mn	0.482	Bal.
Zn-0.8Mn	0.789	Bal.

Table 1. Chemical composition of the obtained casting alloy samples. (*wt*%).

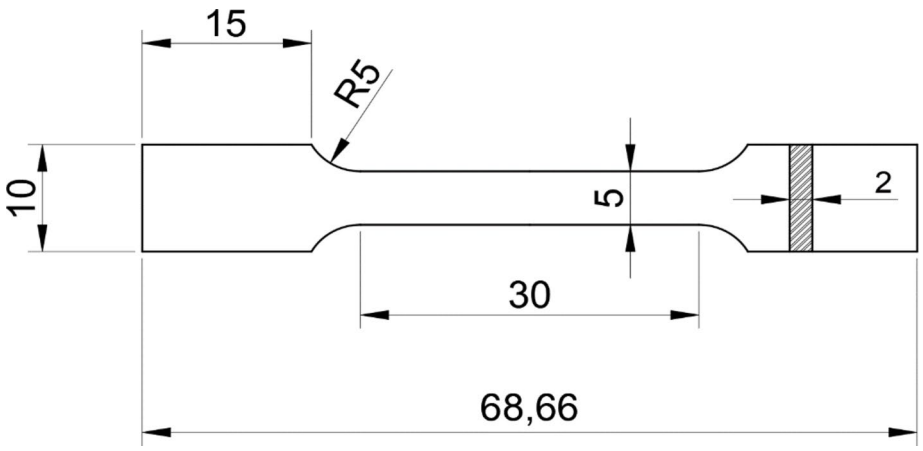

Fig. 1. The dimensions of the tensile test specimens.

using the Cell Counting Kit-8 (CCK-8, Beyotime Biotechnology, China). L929 cells in logarithmic growth phase were counted and seeded into 96-well culture plates after adjusting the cell concentration. The extraction fluid concentrations were 25%, 50% and 100%, and cells were cultured for 24 h, 48 h and 72 h. respectively. After each well was washed twice with phosphate buffered saline (PBS), 100 μL of DMEM medium containing 10% CCK-8 solution was added, and the cells were cultured for 1 h in a 5% CO_2 at 37 ℃ in a constant temperature incubator. The absorbance values of each experimental group were measured at 450 nm using a microplate reader, and the relative cell viability (R) was calculated using the following formula:

$$R = \frac{OD_E - OD_B}{(OD_C - OD_B) \times 100} \times 100\% \quad (1)$$

where ODE represents the absorbance of the experimental group extraction fluid, ODB is the absorbance of the untreated multi-well plate, and ODC refers to the absorbance of the control group extraction fluid.

Electrochemical test

After polishing, the specimens were sealed with epoxy resin, exposing an area of 0.785 cm^2. Electrochemical tests were carried out using an electrochemical workstation (CH310H) in simulated body fluid (SBF) solution at 37 ± 0.5 °C. A standard three-electrode system was employed, with the tested specimen as the working electrode, a saturated calomel electrode as the reference electrode and a platinum sheet electrode as the counter electrode[36]. Prior to the start of testing, the specimens were immersed in SBF solution for 1 h to obtain a relatively stable open-circuit potential. Subsequently, electrochemical impedance spectroscopy (EIS) and potentiodynamic polarization scans were performed. Potentiodynamic polarization curves were measured from − 0.5 V to 0.5 V relative to the open-circuit potential at a scan rate of 0.333 mV/s. The potential polarization curves were measured at a scan rate of 0.333 mV/s. The corrosion rate (CR) of the specimens was calculated using the formula:

$$CR = K\frac{i_{corr}W}{n\rho} \quad (2)$$

where CR represents the corrosion rate (mm/y), K = 3.27 × 10 −3 $m{\cdot}mg{\cdot}\mu A^{-1}{\cdot}cm^{-1}{\cdot}year^{-1}$, I_{corr} refers to the corrosion current density (mA/cm^2), W denotes the atomic mass of the specimen, n indicates the number of transferred electrons, and ρ represents the density of the metal (g/cm^3).

Immersion test

The pre-polished specimens were immersed in ethanol for ultrasonic cleaning, followed by drying and recording the initial weight of the specimens using an electronic balance. Subsequently, the specimens were immersed in a simulated body fluid (SBF) solution consisting of: $NaHCO_3$ (0.345 $g{\cdot}L^{-1}$), Na_2SO_4 (0.075 $g{\cdot}L^{-1}$), $MgCl_2{\cdot}6H_2O$ (0.325 $g{\cdot}L^{-1}$), NaCl (8.015 $g{\cdot}L^{-1}$), KCl (0.255 $g{\cdot}L^{-1}$), $CaCl_2$ (0.285 $g{\cdot}L^{-1}$), $KH_2PO_4{\cdot}3H_2O$ (0.225 $g{\cdot}L^{-1}$), HCl (0.025 $mol{\cdot}L^{-1}$), and Tris (6.228 $g{\cdot}L^{-1}$), where Tris was used as buffer. The pH of the solution was adjusted to 7.4 ~ 7.5 and immersed for 28 days at 37 ± 0.5 °C, maintaining a solution to sample surface area ratio of 1 cm^2:20 mL. To simulate a complete physiological environment, the SBF solution was replaced every 48 h during the 28-day test period to maintain the stability of physiological conditions, and the pH of the solution was recorded every 4 days. Samples were retrieved on days 1, 7, 14, 21 and 28. Ultimately, the specimens were immersed in a 4% nitric acid alcohol solution to remove corrosion products, then rinsed with deionized water, dried and weighed. Finally, the surface morphology of the specimens with and without corrosion products removed was observed using a scanning electron microscope and elemental analyses were carried out using an energy dispersive spectrometer. The corrosion rate (v) of the samples was calculated using the formula:

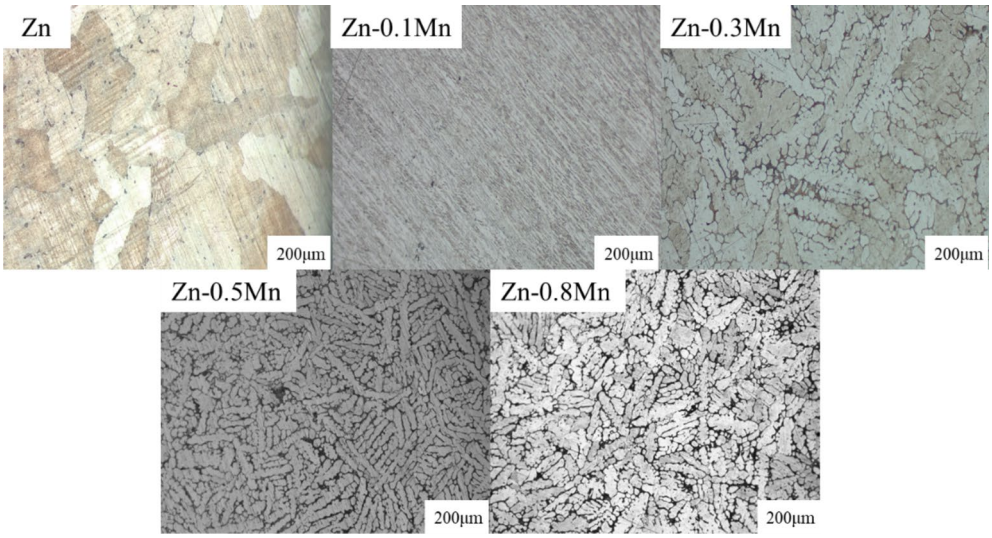

Fig. 2. The microstructures of pure Zn and Zn-Mn alloy.

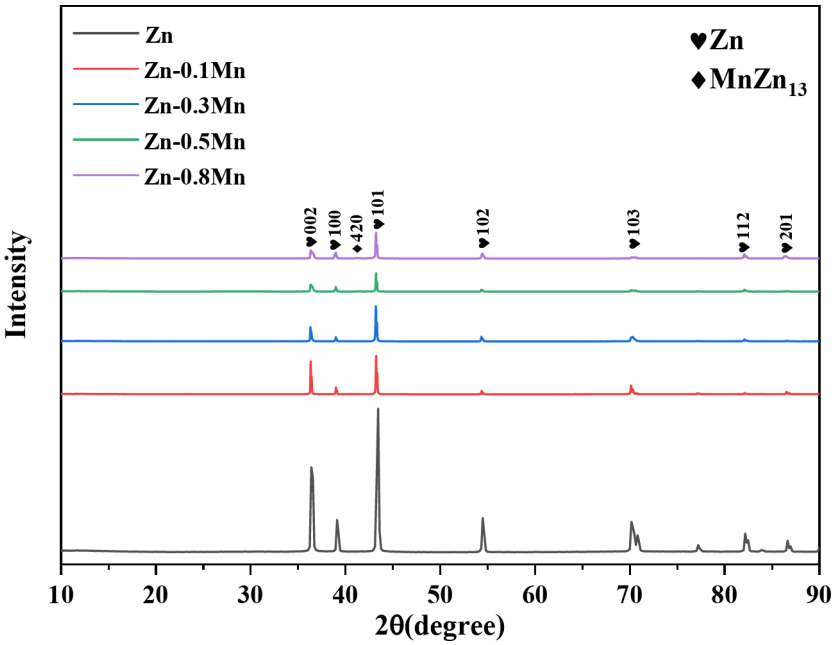

Fig. 3. The XRD patterns of pure Zn and Zn-Mn alloy.

$$v = \frac{\Delta m}{\rho \cdot A \cdot T} \tag{3}$$

where Δm refers to the weight loss of the specimen due to corrosion during immersion (g), A is the exposed surface area of the specimen in the solution (mm^2), T denotes the immersion time (h), and ρ indicates the density of the specimen (g/mm^3). To ensure the accuracy of the experimental data, three parallel specimens were prepared for each experimental group.

Results and discussion

Microstructure

Figure 2 shows the metallographic structure of pure Zn and Zn-Mn alloys. It can be observed from the figure that Zn-Mn alloy is mainly composed of Zn matrix phase and second phase, while the microstructure of pure Zn is mainly composed of elongated plate-like crystals. From the XRD diffraction pattern shown in Fig. 3, it can be concluded that there are almost diffraction peaks of Zn in the spectra of pure Zn and Zn-0.1Mn alloys, indicating that the number of second phases is very small in alloys with low Mn content; When the Mn content

gradually increases to 0.3 *wt*%, diffraction peaks of $MnZn_{13}$ phase can be observed in the spectrum, and as the Mn content gradually increases, the diffraction peaks also continue to strengthen. The second phase in the alloy is mainly $MnZn_{13}$ phase. By observing the phase diagram of the alloy, it can be found that during the equilibrium solidification process, Zn precipitates from the liquid phase. When the temperature drops to the eutectic temperature, Zn and $MnZn_{13}$ phases precipitate from the liquid phase. During the cooling process, due to the rapid temperature drop, the temperature inside the alloy cannot diffuse quickly and effectively, resulting in the segregation of second phases. When the Mn content is 0.1 *wt*%, almost no $MnZn_{13}$ phase is produced in the alloy. But with the continuous increase of Mn content, a small amount of second phase structure appeared in the intermetallic compounds. Due to the preferential precipitation of $MnZn_{13}$ phase over pure Zn phase during equilibrium solidification, it is distributed at the grain boundaries between grains, hindering grain growth and increasing nucleation sites, resulting in more distinct interfaces between grains and gradual grain refinement.

Mechanical properties

Figure 4 shows the Vickers hardness of pure Zn and Zn-Mn alloys. With the increase in Mn content, the hardness of the alloy progressively improves. While the hardness of pure zinc is 43 HV, after addition of Mn, the hardness of Zn-Mn alloys are 54 HV, 69 HV, 78 HV and 70 HV, respectively. According to the Zn Mn phase diagram, the maximum solid solubility of Mn in Zn is 0.2% at a temperature of 160 ℃[37] and a eutectic reaction occurs, leading to the precipitation of the $MnZn_{13}$ phase at 400 °C. Metallographic results indicate that Zn-0.1Mn has almost no second-phase structure, but its hardness is slightly higher than that of pure Zn, which is due to the solid solution strengthening that occurs around 0.1 *wt*% Mn, resulting in a slight improvement in the mechanical properties of the alloy. When the Mn content exceeds 0.3 *wt*%, the $MnZn_{13}$ phase precipitates gradually, leading to the strengthening of the second phase, which further improves the mechanical properties of the alloys due to its homogeneous distribution in the alloys. However, when the Mn content in the alloy exceeds 0.8 wt%, the hardness of the alloy slightly decreases. The reason for this phenomenon be the excessive precipitation of $MnZn_{13}$ phase, which leads to the aggregation and segregation of second phase particles, thereby affecting the integrity of grain boundaries, increasing local brittleness, and reducing the strengthening effect of grain boundaries. In addition, excessive second phases can also cause embrittlement of the alloy, resulting in a slight decrease in hardness.

Figures 5 and 6 depict the yield strength (YS), ultimate tensile strength (UTS), elongation at break, and stress-strain curves of pure Zn and Zn-Mn alloys after tensile testing. The UTS values for pure Zn and Zn-Mn alloys are 45.1 MPa, 84.7 MPa, 97.4 MPa, 117.3 MPa and 103.1 MPa, respectively. It is noteworthy that the tensile strength of pure Zn is significantly increased by the addition of Mn. Among the alloys with different compositions, the UTS of Zn-0.1Mn is lower as compared to the other three alloys, which may be attributed to the relatively low content of the intermediate phase $MnZn_{13}$. The addition of Mn also increases the yield strength of pure Zn, with the YS increasing from 31.5 MPa for pure Zn to a maximum value of 110.4 MPa for Zn-0.5Mn alloy. In addition, the YS of the other three alloys also increased in different degrees. The trend of elongation at break is similar to that of UTS and YS, with alloying leading to higher elongations of 6%, 11.6%, 12.8% and 14.3%, respectively, compared to pure Zn. Notably, the elongation at fracture continues to increase even when the Mn content reaches 0.8 *wt*%. Overall, the mechanical properties of the alloys improve with increasing Mn content due to the precipitation of the intermediate phase $MnZn_{13}$ at grain boundaries, leading to grain boundary strengthening. However, similar to the microhardness, the overall mechanical properties of the alloys decrease slightly when the Mn content reaches 0.8 *wt*%.

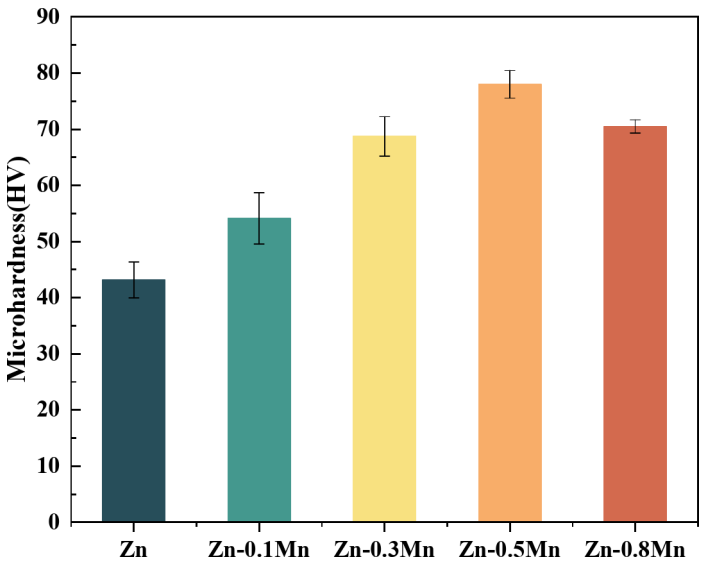

Fig. 4. The microhardness of Zn and Zn-Mn alloy.

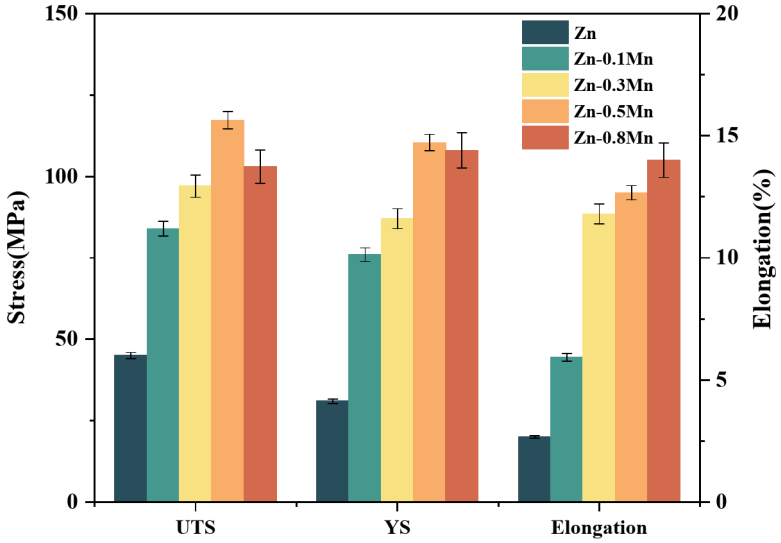

Fig. 5. The mechanical properties of pure Zn and Zn-Mn alloy.

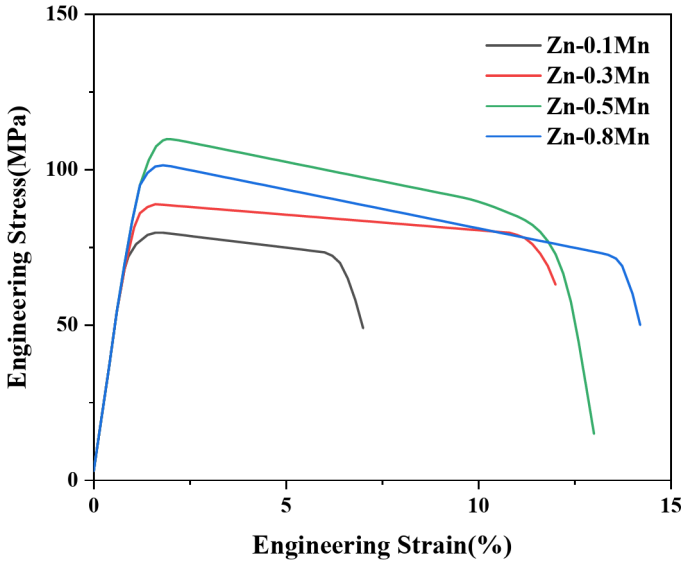

Fig. 6. Stress strain curve of Zn-Mn alloy.

Antibacterial testing

Figure 7 shows the results of antimicrobial testing of pure Zn and Zn-Mn alloys. The zones of inhibition of pure Zn and Zn-Mn alloys against E. coli were found to be 7.14 mm, 9.48 mm, 9.63 mm, 9.86 mm and 10.69 mm in size, respectively. The Zn-Mn alloys prepared by addition of Mn elements showed improved resistance to E. coli as compared to pure Zn and this improvement was attributed to the synergistic effect of the antimicrobial properties of Zn^{2+} and Mn^{2+}. When the alloy comes into contact with a liquid, the ions contained therein gradually dissolve, and Zn^{2+} and Mn^{2+} bind to enzymes in the bacteria, which play a vital role in their metabolism. Inhibition of enzyme activity interferes with the normal metabolism of bacteria, thus inhibiting bacterial activity and improving the antibacterial properties of the alloys. The dimensions of the inhibition zones of pure Zn and Zn-Mn alloys against. aureus were 10.37 mm, 12.77 mm, 13.95 mm, 13.31 mm and 12.48 mm, respectively. Similar to the case of Escherichia coli, Zn-Mn alloys prepared by addition of Mn were also more resistant to Staphylococcus aureus than pure Zn alloys. However, the antimicrobial properties slightly decreased when the Mn content reached 0.8 *wt*%, which may be attributed to the increase in precipitation of the $MnZn_{13}$ phase at the grain boundaries, resulting in a decrease in the number of Zn^{2+} ions.

In vitro cytotoxicity testing

Figure 8 shows the cell viability of L-929 cells cultured in pure and Zn-Mn alloy at concentrations of 25%, 50% and 100% extracts after 24, 48 and 72 h. At 24 h, the cell viability of all samples at 50% and 25% extract

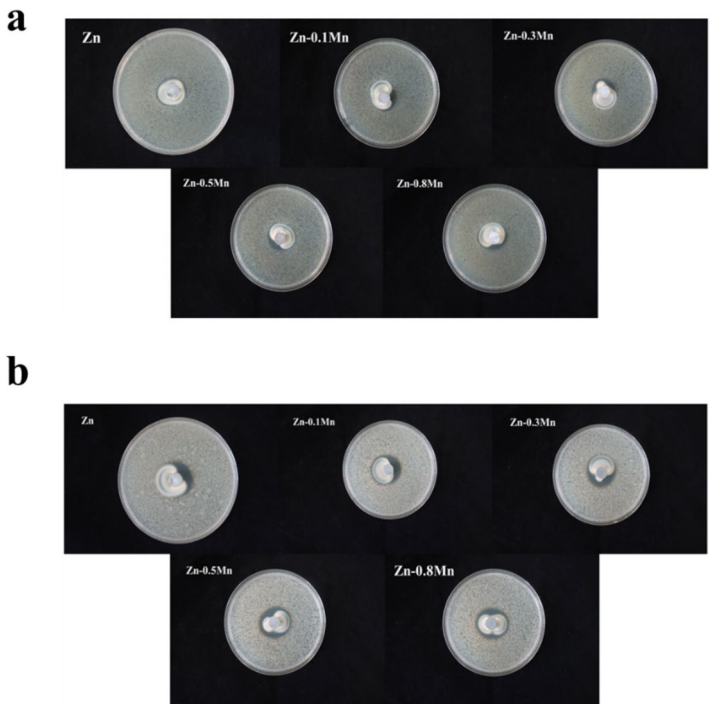

Fig. 7. Antibacterial zone tests for pure Zn and Zn-Mn alloys. (**a**) Inhibition zones against Escherichia coli. (**b**) Inhibition zones against Staphylococcus aureus.

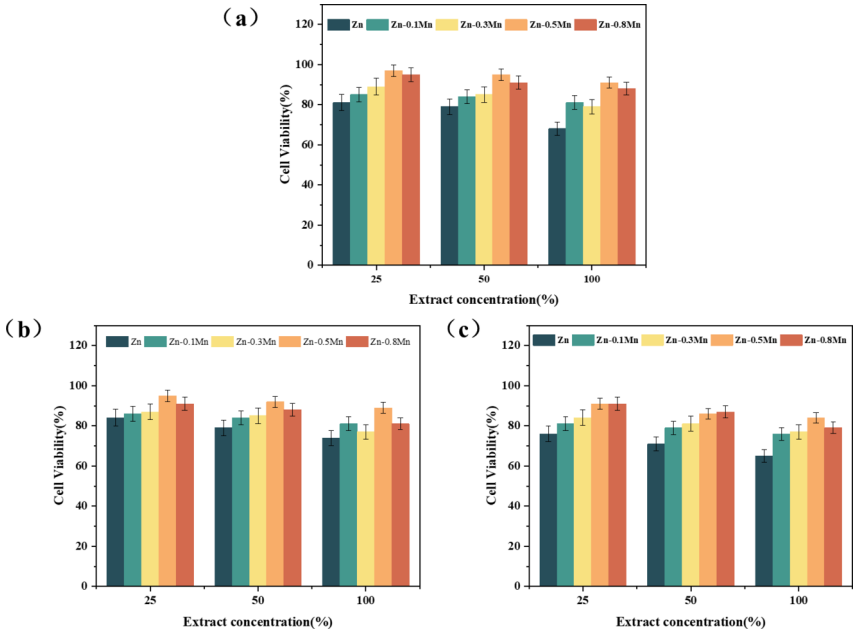

Fig. 8. Survival of L-929 cells in pure zinc and Zn-Mn alloy extracts at concentrations of 25%, 50% and 100%. (**a**) Co-cultured for 24 h. (**b**) Co-cultured for 48 h. (**c**) Co-cultured for 72 h.

concentrations was above the 75% required by the ISO 19003-5 standard[38], while at 100% concentration, all alloys except pure Zn met the standard. Comparative analysis showed that cell viability was higher in Zn-Mn alloy extracts than in pure Zn, with a general trend of decreasing cell viability as the concentration of the extracts increased. Subsequently, after 48 and 72 h of incubation, the situation was similar to that at 24 h, with higher cell viability in Zn-Mn alloy than in pure Zn. Among them, the Zn-0.5Mn alloy showed better cell viability than the other alloys. In summary, the addition of Mn elements reduced the cytotoxicity of pure Zn and showed

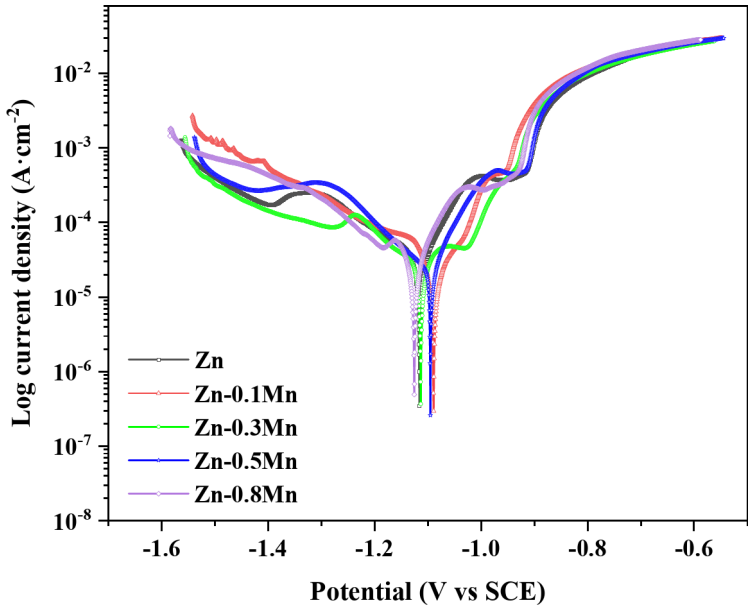

Fig. 9. Polarization curves of Zn-Mn alloys in simulated body fluid (SBF) solution at 37 °C.

Alloys	E_{corr} (V vs. SCE)	I_{corr} (μA/cm²)	Corrosion rate (mm/y)	R_p (kΩ·cm²)	ba (mV/dec)	-bc (mV/dec)
Zn	−1.17	41.37	0.34	38.61	79.69	165.37
Zn-0.1Mn	−1.14	36.70	0.26	43.15	81.06	117.92
Zn-0.3Mn	−1.11	15.07	0.17	49.07	97.40	97.44
Zn-0.5Mn	−1.10	11.26	0.13	52.16	100.93	68.93
Zn-0.8Mn	−1.13	23.29	0.21	47.31	97.74	81.33

Table 2. Fitted electrochemical parameters.

greater cytocompatibility. Although the cell viability decreased slightly with increasing extract concentration and incubation time, it was still within the acceptable standard range (> 75%).

Electrochemical test

Figure 9 shows the polarization curves of pure Zn and Zn-Mn alloys in SBF simulated body fluid at 37 °C. It can be seen from the curves that there is a plateau in the anodic region indicating that the corrosion type of the alloys is mainly pitting corrosion. The reaction of the Zn alloys in the SBF simulated body fluid is[39]:

$$Zn + 2H_2O = Zn^{2+} + 2OH^- + H_2\uparrow \quad (4).$$

By observing the Pourbaix diagram of Zn alloys, it can be found that pure Zn or Zn alloys are more prone to passivation reactions in neutral or weakly alkaline solutions[40]. In the anode region of the curve, the corrosion current density (I_{corr}) slowly increases with the increase of corrosion potential (E_{corr}). This may be due to the poor quality of the passivation film in the early stages of its formation, which did not provide very effective protection before being destroyed. As the potential (E) further increases, the passivation film is broken down, resulting in a significant increase in corrosion current density. When the content of Mn element in the alloy increases to 0.3 *wt*% and 0.5 *wt*%, the curve shows a clear "step", indicating that the alloy has formed a relatively dense passivation film during the reaction process. However, the passivation reaction of Zn-0.5Mn alloy occurs at higher corrosion potentials, and the passivation film is damaged as the potential further increases. The fitting was conducted using the Levenberg-Marquardt nonlinear least squares fitting method, employing C-view software for fitting the polarization curves. The results are presented in Table 2. The addition of Mn element increases the corrosion current density (I_{corr}) and corrosion potential (E_{corr}) to varying degrees. From the perspective of corrosion potential, pure Zn has the most negative corrosion potential, indicating that under the same medium environment, pure Zn is most prone to corrosion; However, with the addition of Mn element, the corrosion potential of the alloy gradually becomes more negative, indicating that Mn element has a relatively positive impact on the chemical stability of the alloy. The corrosion current density of the alloy increased from 11.26 μA/cm² for Zn-0.5Mn to 41.37 μA/cm² for pure Zn, indicating that the addition of Mn element resulted in the formation of a dense passivation film on the alloy in the solution medium. In addition, we analyzed the polarization resistance (R_p) using Stern and Geary relationships, and the results showed that the order of change in alloy R_p values was Zn-0.5Mn > Zn-0.3Mn > Zn-0.8Mn > Zn-0.1Mn > Zn. R_p indicates the degree of difficulty of the reaction, and a larger Rp indicates that the electrochemical reaction occurring on the alloy surface is more

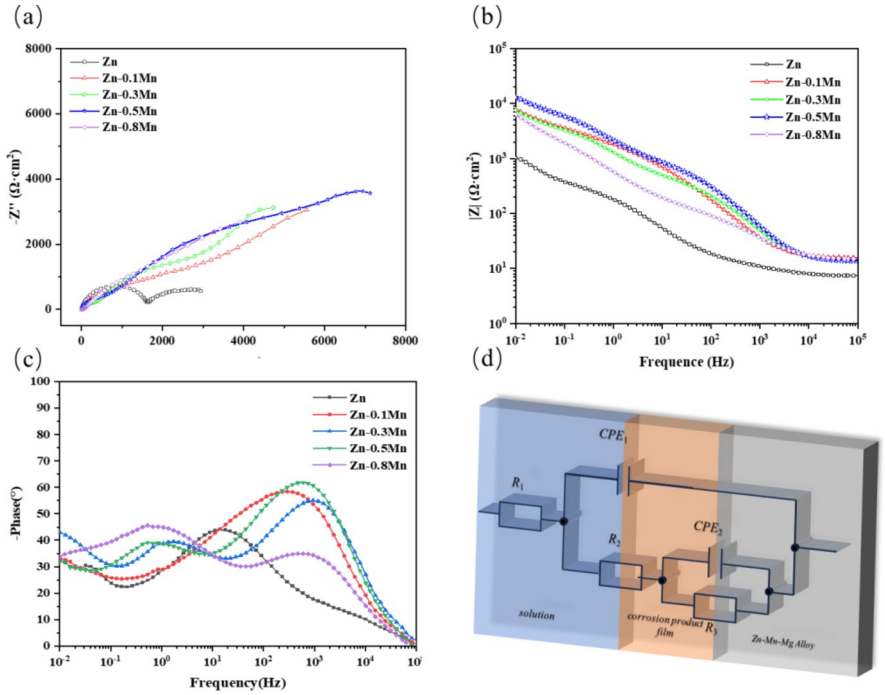

Fig. 10. Electrochemical impedance spectroscopy (EIS) plots of Zn-Mn alloy in SBF solution at 37 °C. (**a**) Nyquist plot; (**b**) Bode modulus plot; (**c**) Bode phase angle plot; (**d**) Equivalent circuit diagram.

Alloys	R_1 ($\Omega \cdot cm^2$)	CPE_1-T ($S^n \cdot \Omega^{-1} \cdot cm^{-2}$)	CPE_1-P ($S^n \cdot \Omega^{-1} \cdot cm^{-2}$)	R_2 ($\Omega \cdot cm^2$)	CPE_2-T ($S^n \cdot \Omega^{-1} \cdot cm^{-2}$)	CPE_2-P ($S^n \cdot \Omega^{-1} \cdot cm^{-2}$)	R_3 ($\Omega \cdot cm^2$)
Zn	19.44	2.79×10^{-5}	0.71	38.72	3.32×10^{-4}	0.44	6029
Zn-0.1Mn	18.91	2.41×10^{-5}	0.81	39.16	1.48×10^{-4}	0.67	6671
Zn-0.3Mn	15.87	3.80×10^{-5}	0.76	40.35	2.85×10^{-4}	0.59	7182
Zn-0.5Mn	14.04	1.91×10^{-5}	0.85	42.69	3.07×10^{-4}	0.60	7496
Zn-0.8Mn	18.60	1.57×10^{-5}	0.74	40.29	4.93×10^{-4}	0.65	7246

Table 3. Fitting data of each component in the equivalent circuit.

difficult to carry out, which is consistent with the results of corrosion rate. By observing the anodic polarization coefficient (ba) and cathodic polarization coefficient (bc) of the alloy, it was found that the ba value of Zn-0.5Mn alloy was the highest and the bc value was the lowest. This indicates that the anodic reaction of the alloy was suppressed during the reaction process, while the cathodic reaction was relatively fast. This may be due to the dense passivation film generated by the alloy in the solution effectively suppressing the anodic dissolution reaction, and the entire corrosion process was dominated by cathodic reaction, thereby slowing down the overall corrosion rate.

Using EIS, the corrosion behavior of the Zn-Mn alloy was evaluated and the equivalent circuit, Nyquist plot and Bode plot are shown in Fig. 10. The Bode diagram shows a relatively long plateau, so the equivalent circuit of the system should be a double layer structure. Figure 10 (d) is an equivalent circuit diagram consisting of solution resistance R_1, membrane resistance R_2, charge transfer resistance R_3, double-layer capacitor CPE_1, and capacitor CPE_2 representing corrosion products. It can be seen that after adding a certain amount of Mn element to the alloy, the capacitance arc radius in the Nyquist plot and the impedance modulus value | Z | in the Bode plot of the alloy both increased, indicating that the corrosion resistance of the alloy has been improved to a certain extent. The EIS results were fitted using Z-View software, and the results are shown in Table 3. From the fitted data, it can be seen that the CPE_1 value (1.91×10^{-5}) of the double-layer capacitance of Zn-0.5Mn alloy is significantly lower than that of alloys with lower pure Zn and Mn content, indicating the formation of a more stable passivation film on the alloy surface. Mn, as an alloying element, promotes the formation of the oxide film and improves the stability of the passivation film to a certain extent. Among the five metals tested, pure Zn has the lowest charge transfer resistance R_3, indicating that charge transfer occurs faster and corrosion is more severe on the surface of pure Zn in solution. Overall, after adding Mn element to Zn to form an alloy, the degradation rate was slowed down to a certain extent, and the order of degradation rate is as follows: Zn > Zn-0.1Mn > Zn-0.8Mn > Zn-0.3Mn > Zn-0.5Mn. The degradation rate of Zn-0.5Mn alloy is the slowest among the four alloys.

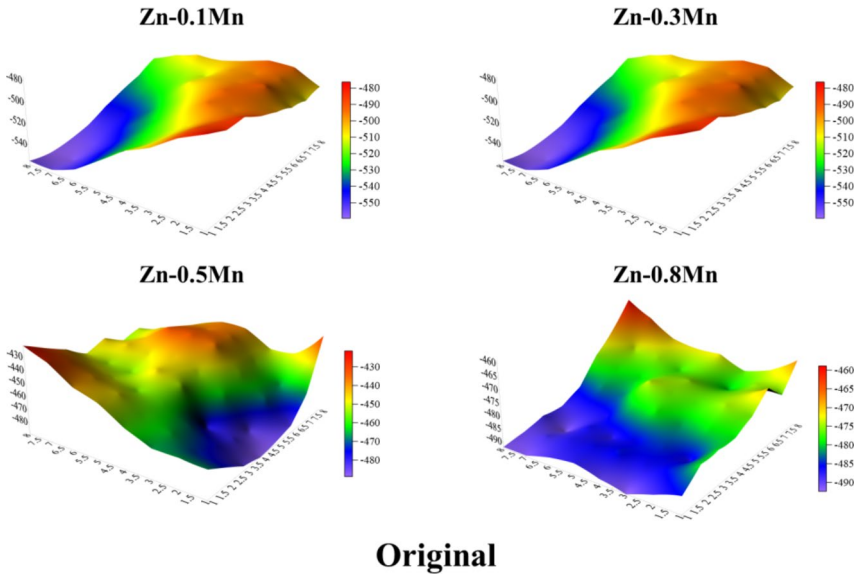

Fig. 11. Potential distribution on the surface of Zn-Mn alloys in the initial state.

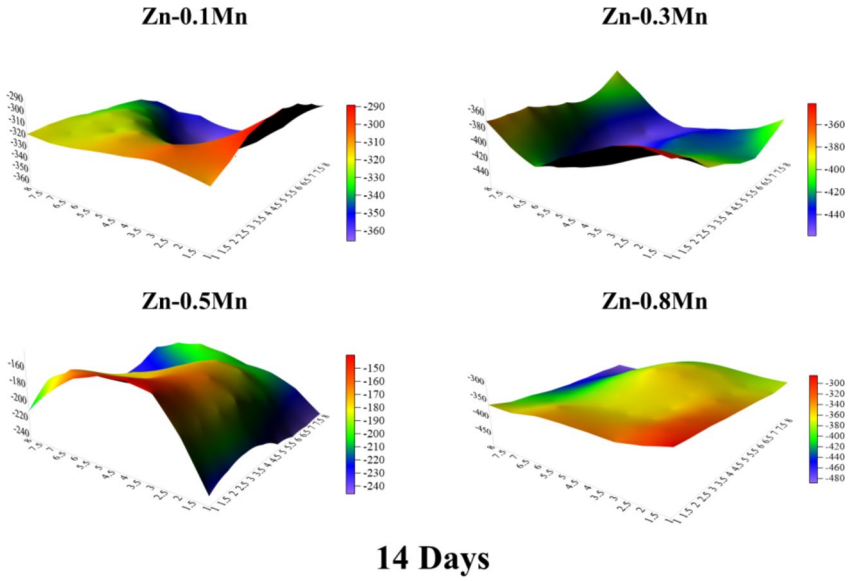

Fig. 12. Potential distribution on the surface of Zn-Mn alloys after 14 days of immersion.

Scanning Kelvin probe testing

The scanning Kelvin probe was used to measure the work function of the sample surface, which describes the ease with which electrons can escape from the metal surface. Higher volt potential indicates that the material is less susceptible to corrosion. Figures 11, 12 and 13 show the surface potential distribution of Zn-Mn alloys for different immersion times. Before corrosion by immersion, the Zn-0.3Mn alloy has the highest average Volta potential of about −237 mV. After 14 days of immersion, the average Volta potential of Zn-0.5Mn increased to -193 mV, which was attributed to the fact that the film of corrosion products produced during immersion covered the metal surface, thus hindering the diffusion process and slowing down the corrosion rate. After 28 days of immersion, the volt potentials of all four alloy compositions decreased to varying degrees, but were still higher than those of the unimmersed alloys, and it was hypothesised that this could be due to the damage caused to the corrosion product film by ionic attack. In conclusion, the corrosion product film generated during immersion has a certain protective effect on the substrate.

Immersion test

Figure 14 illustrates the degradation rates of Zn-Mn alloys and pure Zn after immersion in simulated body fluid (SBF) at 37 °C for 1, 7, 14, 21 and 28 days. It can be observed that by the 7th day of immersion, all four alloys

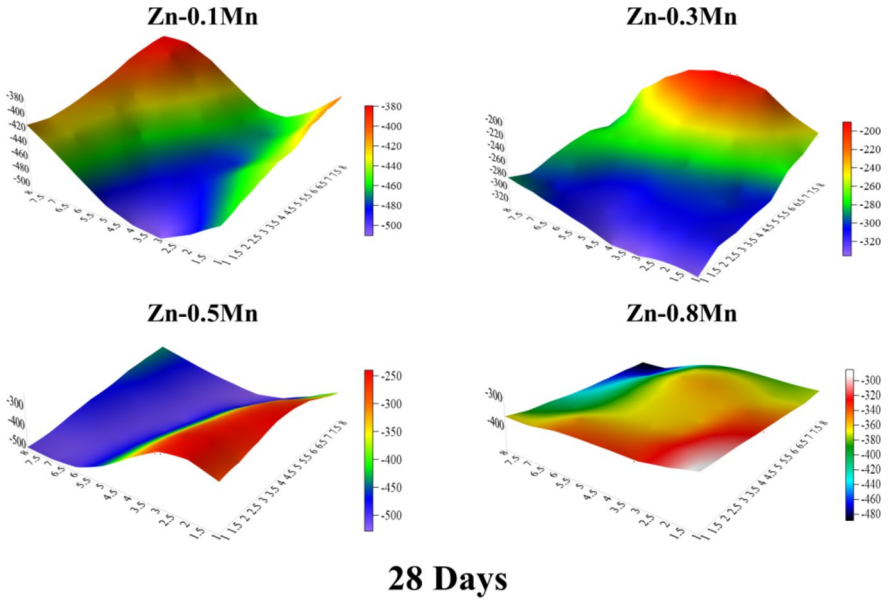

Fig. 13. Potential distribution on the surface of Zn-Mn alloys after 28 days of immersion.

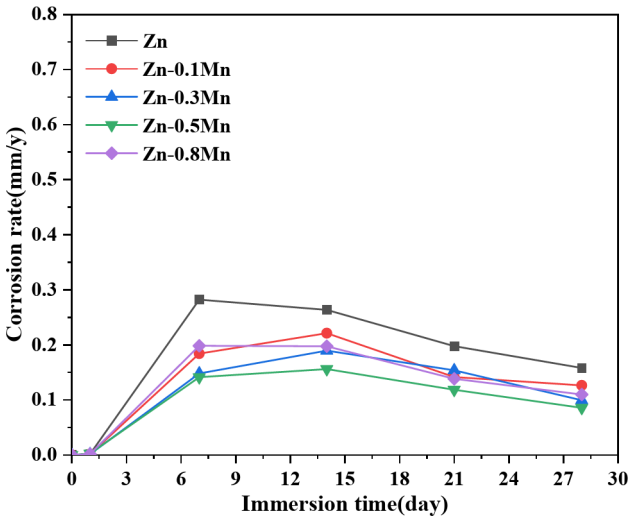

Fig. 14. The corrosion rates of Zn-Mn alloy and pure Zn in SBF solution at 37 °C.

and It can be seen that the corrosion rates of all four alloys and pure Zn increase significantly on the 7th day of immersion, with Zn-0.8Mn having a relatively slow corrosion rate of 0.028 mm/y. The overall corrosion rate continues to increase as the immersion time increases. However, the slower incremental rate of corrosion for the Zn-0.3Mn and Zn-0.5Mn alloys suggests that rapid corrosion in the early stages of immersion leads to the formation of a more compact layer of corrosion products compared to the other manganese-containing alloys. By reducing the contact area with the solution, this layer reduces the corrosion rate. In general, the overall corrosion rate of Zn-Mn alloys is slightly reduced by the addition of Mn elements. This is also related to the quantity and distribution of $MnZn_{13}$ phase in Zn-Mn alloy. During the soaking process, $MnZn_{13}$ phase, as a strengthening phase, mainly precipitates at the grain boundaries or in the matrix of the alloy. The second phase precipitated at the grain boundaries strengthens the alloy and acts as a barrier to the invasion of the solution. In addition, although the second phase particles distributed at the matrix cannot completely cover the surface of the alloy, they can promote the generation of corrosion products on the alloy surface and slow down the corrosion of the alloy to a certain extent.

Figure 15 shows the corrosion morphology of Zn-Mn alloys after immersion in SBF solution at 37 ± 0.5 °C for 28 days. It can be seen that the surface of the immersed Zn-Mn alloy is covered with a large number of white flocculent corrosion products. The corrosion products of the Zn-0.3Mn alloy are relatively dispersed, As shown by the red box in Fig. 15 (b), which indicates that the protection of the substrate during the corrosion

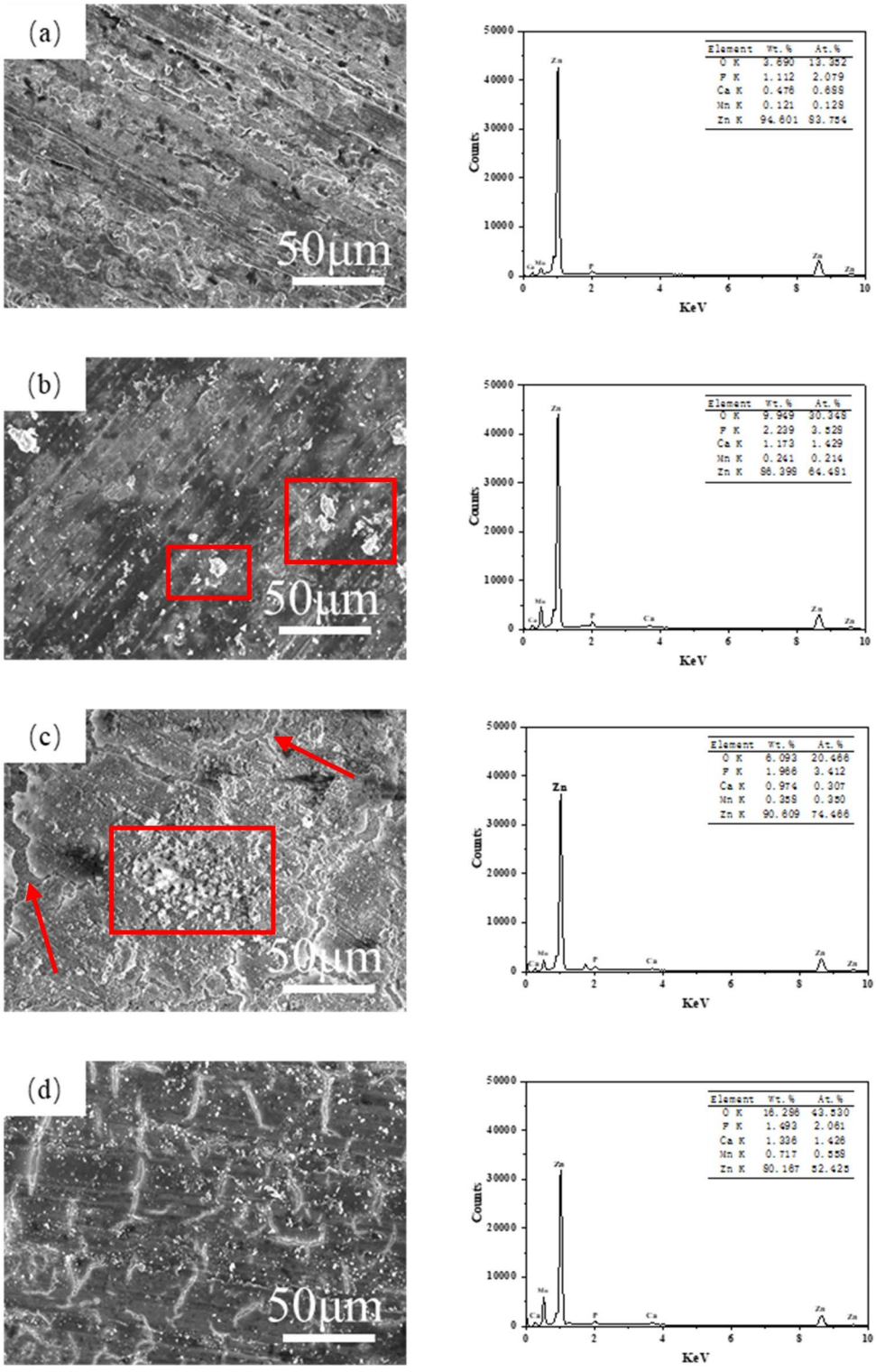

Fig. 15. SEM images and EDS results of Zn-Mn alloys after 28 days of immersion in SBF (simulated body fluid) solution at 37 °C. (**a**) Zn-0.1Mn, (**b**) Zn-0.3Mn, (**c**) Zn-0.5Mn and (**d**) Zn-0.8Mn.

process is weak, while the corrosion products of the Zn-0.5Mn are more compact, of which is in agreement with the corrosion rate analyzed previously. However, it was clearly observed that the corrosion product layer had cracked, as indicated by the red arrow in the figure. EDS analysis of the surface corrosion products reveals the presence of elements such as Zn, Mn, Ca, P and O. This suggests that in addition to the alloying elements and alkaline oxides, the corrosion products may contain compounds such as $Zn_3(PO_4)_2{\cdot}4H_2O$[41] or $ZnHPO_4$[42]. Such compounds in pure zinc may play a role in slowing down corrosion[43] and promoting osteoblast proliferation[44].

Figure 16 depicts the surface morphology of the zinc-manganese alloys after removal of the corrosion products after 28 days of immersion, and it is evident that many corrosion pits have formed as a result of the corrosion. The corrosion of alloys with Mn content below 0.5 *wt*% is relatively uniform and there are no severe corrosion pits. Nevertheless, when the Mn content reaches 0.8 *wt*%, the detachment of $MnZn_{13}$ phases leads to the formation of uneven and more pronounced corrosion pits on the surface of the alloy.

In vitro degradation behavior of Zn-Mn alloy

According to the experimental results presented earlier, the corrosion of Zn-Mn alloys in simulated body fluids (SBF) can be attributed to the following processes. Initially, the following reactions occur when Zn-Mn alloys are immersed in simulated body fluids:

$$\text{Anode reaction}: Zn \rightarrow Zn^{2+} + 2e^{-} \tag{5}$$

$$\text{Cathode reaction}: O_2 + H_2O + 4e^{-} \rightarrow 4OH^{-} \tag{6}$$

$$\text{Formation of } 2Zn(OH)_2: 2Zn^{2+} + 4OH^{-} \rightarrow 2Zn(OH)_2 \tag{7}$$

$$\text{Formation of } 2ZnO: Zn(OH)_2 \rightarrow ZnO + H_2O \tag{8}$$

$$\text{Formation of } Zn_3(PO_4)_2: 3Zn^{2+} + 2OH^{-} + 2H_2O + 2HPO_4{}^{2-} \rightarrow Zn_3(PO_4)_2 \cdot 4H_2O \tag{9}$$

The corrosion mechanism is shown in Fig. 17. In the simulated body fluid, ions such as Ca^{2+} and $PO_4{}^{3-}$ undergo replacement reactions with metal ions and form tiny flocculent corrosion products on the metal surface. Subsequently, these corrosion products are gradually adsorbed and deposited at the interface between the metal and the solution. As the immersion time increases, the deposition of these products increases, thereby reducing the contact area between the solid and the liquid, and thus reducing the corrosion rate. However, as the corrosion products continue to accumulate, the effect of surface tension causes cracks to appear in the layer of corrosion products, which results in the solution coming back into contact with the surface of the alloy, again accelerating the corrosion process. Over time, the cracks in the corrosion product layer widen until they detach from the metal surface, and so on.

Conclusion

In the present study, Zn-xMn (x = 0.1, 0.3, 0.5 and 0.8 *wt*%) alloys were prepared and characterised for their mechanical properties, microstructure, in vitro corrosion behaviour, cytotoxicity and antibacterial properties. In addition, the effect of different manganese element contents on various properties of the alloys has been investigated. The main conclusions are as follows:

(1) Through metallographic observation and XRD analysis of the alloy, it was found that the addition of Mn element resulted in the appearance of $MnZn_{13}$ phase in the alloy, and with the continuous increase of Mn content, the number of second phases in the alloy also gradually increased. These $MnZn_{13}$ phases distributed in the alloy have significantly improved the mechanical properties of the alloy. And subsequent immersion

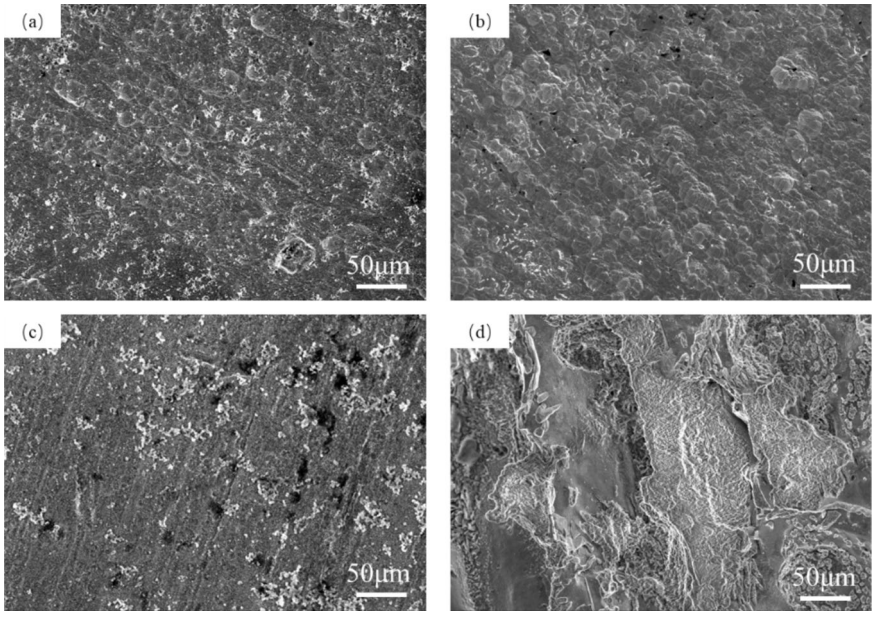

Fig. 16. The surface morphology of Zn-Mn alloys after removal of corrosion products after 28 days of immersion in SBF (simulated body fluid) solution at 37 °C. (**a**) Zn-0.1Mn, (**b**) Zn-0.3Mn, (**c**) Zn-0.5Mn and (**d**) Zn-0.8Mn.

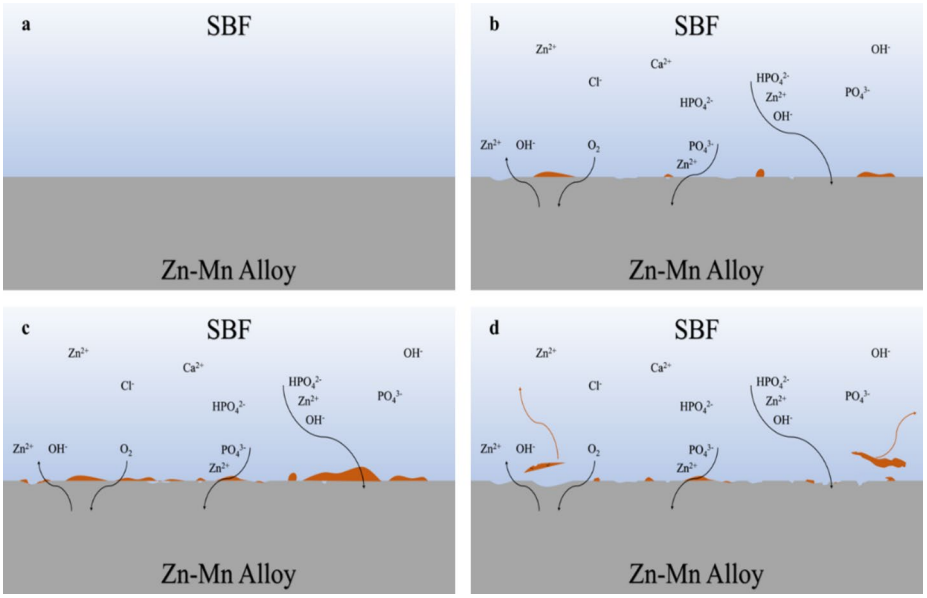

Fig. 17. Schematic diagram of the corrosion process of Zn-Mn alloy in SBF solution. (**a**) Initial state. (**b**) Preliminary formation of corrosion products. (**c**) Large amount of corrosion products adhering to the surface of the alloy. (**d**) Cracking and detachment of the corrosion product layer.

experiments have shown that the corrosion resistance of $MnZn_{13}$ relative to the alloy has also been improved to a certain extent.

(2) The results of immersion tests indicate that the addition of Mn elements reduces the corrosion rate of pure Zn in simulated body fluid (SBF). The corrosion rate is characterized by a rapid increase in the initial period of immersion, followed by a deceleration with the formation of the corrosion product layer on the surface of the alloy, a trend that was confirmed by subsequent electrochemical and scanning Kelvin probe tests. EDS analyses of the corrosion products reveals the presence of elements such as Zn, Mn, O, Ca and P.

(3) The antimicrobial properties of Zn-Mn alloys (against Escherichia coli and Staphylococcus aureus) are superior compared to pure Zn. In addition, in vitro cytotoxicity tests show that cell survival in Zn-Mn alloy extracted solutions is higher than that in pure Zn and remains within acceptable standards (> 75%). Therefore, the addition of small amounts of manganese is not detrimental to cells.

Overall, Zn-Mn alloys prepared by melting under Ar gas atmosphere protection have significantly improved mechanical properties, corrosion resistance, and biocompatibility compared to pure Zn after homogenization treatment. Zn-Mn alloys prepared by this method are expected to become potential biodegradable alloy materials.

Data availability

Data will be made available on request. The data that support the findings of this study are available from the corresponding author, [Dalei Zhang], upon reasonable request.

Received: 3 January 2025; Accepted: 5 March 2025
Published online: 15 March 2025

References

1. Al-Shalawi, F. D. et al. Biodegradable synthetic polymer in orthopaedic application: A review. *Mater. Today: Proc.* **74**, 540–546 (2023).
2. Zheng, Y. F., Gu, X. N. & Witte, F. Biodegradable metals. *Mater. Sci. Engineering: R: Rep.* **77**, 1–34 (2014).
3. Windhagen, H. et al. Biodegradable magnesium-based screw clinically equivalent to titanium screw in hallux valgus surgery: short term results of the first prospective, randomized, controlled clinical pilot study. *Biomed. Eng. Online.* **12**, 62 (2013).
4. Song, B. et al. Biomechanical comparison of pure magnesium interference screw and polylactic acid polymer interference screw in anterior cruciate ligament reconstruction—A cadaveric experimental study. *J. Orthop. Translation*. **8**, 32–39 (2017).
5. Peng, Q., Li, X., Ma, N., Liu, R. & Zhang, H. Effects of backward extrusion on mechanical and degradation properties of Mg–Zn biomaterial. *J. Mech. Behav. Biomed. Mater.* **10**, 128–137 (2012).
6. Chou, D. T. et al. Novel processing of iron–manganese alloy-based biomaterials by inkjet 3-D printing. *Acta Biomater.* **9**, 8593–8603 (2013).
7. Lin, W. et al. Long-term in vivo corrosion behavior, biocompatibility and bioresorption mechanism of a bioresorbable nitrided iron scaffold. *Acta Biomater.* **54**, 454–468 (2017).
8. Drynda, A., Hassel, T., Bach, F. W. & Peuster, M. In vitro and in vivo corrosion properties of new iron–manganese alloys designed for cardiovascular applications. *J. Biomedical Mater. Res. Part. B: Appl. Biomaterials.* **103**, 649–660 (2015).
9. Hermawan, H., Purnama, A., Dube, D., Couet, J. & Mantovani, D. Fe–Mn alloys for metallic biodegradable stents: degradation and cell viability studies. *Acta Biomater.* **6**, 1852–1860 (2010).

10. Niu, J. et al. The in vivo degradation and bone-implant interface of Mg-Nd-Zn-Zr alloy screws: 18 months post-operation results. *Corros. Sci.* **113**, 183–187 (2016).
11. Kaviani, M., Ebrahimi, G. R. & Ezatpour, H. R. Improving the mechanical properties and Biocorrosion resistance of extruded Mg-Zn-Ca-Mn alloy through hot deformation. *Mater. Chem. Phys.* **234**, 245–258 (2019).
12. Riaz, M., Najam, M., Imtiaz, H., Bashir, F. & Hussain, T. Structural and biological analysis of Zn–Cu based biodegradable alloys for orthopedic application. *Mater. Chem. Phys.* **312**, 128618 (2024).
13. Siswayanti, B. et al. Corrosion Inhibition induced by Captopril in Hanks' solution on bioresorbable Mg–Zn-(Y, Nd) alloys fabricated by powder metallurgical technology. *Mater. Chem. Phys.* **313**, 128705 (2024).
14. Xie, Y. et al. Fabrication and properties of porous Zn-Ag alloy scaffolds as biodegradable materials. *Mater. Chem. Phys.* **219**, 433–443 (2018).
15. Tang, Z. et al. Design and characterizations of novel biodegradable Zn-Cu-Mg alloys for potential biodegradable implants. *Mater. Design*. **117**, 84–94 (2017).
16. Bowen, P. K., Drelich, J. & Goldman, J. Zinc exhibits ideal physiological corrosion behavior for bioabsorbable stents. *Adv. Mater.* **25**, 2577–2582 (2013).
17. Seitz, J. M., Durisin, M., Goldman, J. & Drelich, J. W. Recent advances in biodegradable metals for medical sutures: A critical review. *Adv. Healthc. Mater.* **4**, 1915–1936 (2015).
18. Du, H., Wei, Z., Liu, X. & Zhang, E. Effects of Zn on the microstructure, mechanical property and bio-corrosion property of Mg–3Ca alloys for biomedical application. *Mater. Chem. Phys.* **125**, 568–575 (2011).
19. Zhang, X. et al. Effects of bovine serum albumin on the corrosion behavior of biodegradable Zn–Cu alloy under dynamic flowing conditions. *Mater. Chem. Phys.* **304**, 127838 (2023).
20. Li, P. et al. Mechanical characteristics, in vitro degradation, cytotoxicity, and antibacterial evaluation of Zn-4.0Ag alloy as a biodegradable material. *Int. J. Mol. Sci.* **19**, 755 (2018).
21. Shi, Z. Z. et al. Design biodegradable Zn alloys: second phases and their significant influences on alloy properties. *Bioactive Mater.* **5**, 210–218 (2020).
22. Yue, R. et al. In vitro cytocompatibility, hemocompatibility and antibacterial properties of biodegradable Zn-Cu-Fe alloys for cardiovascular stents applications. *Mater. Sci. Engineering: C*. **113**, 111007 (2020).
23. Tang, Z. et al. Potential biodegradable Zn-Cu binary alloys developed for cardiovascular implant applications. *J. Mech. Behav. Biomed. Mater.* **72**, 182–191 (2017).
24. Yang, L. et al. Effect of Mg contents on the microstructure, mechanical properties and cytocompatibility of degradable Zn-0.5Mn-xMg alloy. *J. Funct. Biomaterials*. **14**, 195 (2023).
25. Sotoudeh Bagha, P., Khaleghpanah, S., Sheibani, S., Khakbiz, M. & Zakeri, A. Characterization of nanostructured biodegradable Zn-Mn alloy synthesized by mechanical alloying. *J. Alloys Compd.* **735**, 1319–1327 (2018).
26. Yang, L. et al. Influence of Mg on the mechanical properties and degradation performance of as-extruded ZnMgCa alloys: in vitro and in vivo behavior. *J. Mech. Behav. Biomed. Mater.* **95**, 220–231 (2019).
27. Guo, H., He, Y., Zheng, Y. & Cui, Y. In vitro studies of biodegradable Zn-0.1Li alloy for potential esophageal stent application. *Mater. Lett.* **275**, 128190 (2020).
28. ERCETIN, A. *ERCETIN A. A Novel Mg-Sn-Zn-Al-Mn Magnesium Alloy With Superior Corrosion Properties [J]*118– (Metallurgical Research & Technology, 2021). 5.
29. ERCETIN A, ÖZGüN Ö, ASLANTAS K, et al. The microstructure, degradation behavior and cytotoxicity effect of Mg–Sn–Zn alloys in vitro tests [J]. *SN Appl. Sci.* **2**(2), 173 (2020).
30. ERCETIN, A., PIMENOV, D. Y. & Microstructure Mechanical, and Corrosion Behavior of Al2O3 Reinforced Mg2Zn Matrix Magnesium Composites [J]. Materials, (17). (2021).
31. Sun, S. et al. Abnormal effect of Mn addition on the mechanical properties of as-extruded Zn alloys. *Mater. Sci. Engineering: A*. **701**, 129–133 (2017).
32. Liu, X. et al. Micro-alloying with Mn in Zn–Mg alloy for future biodegradable metals application. *Mater. Design*. **94**, 95–104 (2016).
33. Hou, L. et al. Microstructure, mechanical properties, corrosion behavior and biocompatibility of As-Extruded biodegradable Mg–3Sn–1Zn–0.5Mn alloy. *J. Mater. Sci. Technol.* **32**, 874–882 (2016).
34. Shi, Z. Z., Yu, J. & Liu, X. F. Microalloyed Zn-Mn alloys: from extremely brittle to extraordinarily ductile at room temperature. *Mater. Design*. **144**, 343–352 (2018).
35. Jia, B. et al. In vitro and in vivo studies of Zn-Mn biodegradable metals designed for orthopedic applications. *Acta Biomater.* **108**, 358–372 (2020).
36. Ozga, P. & Bielańska, E. Determination of the corrosion rate of Zn and Zn–Ni layers by the EDS technique. *Mater. Chem. Phys.* **81**, 562–565 (2003).
37. Zhu, X. et al. Strengthening mechanism and biocompatibility of degradable Zn-Mn alloy with different Mn content. *Mater. Today Commun.* **31**, 103639 (2022).
38. Qu, X. et al. Biodegradable Zn–Cu alloys show antibacterial activity against MRSA bone infection by inhibiting pathogen adhesion and biofilm formation. *Acta Biomater.* **117**, 400–417 (2020).
39. Vojtěch, D., Kubásek, J., Šerák, J. & Novák, P. Mechanical and corrosion properties of newly developed biodegradable Zn-based alloys for bone fixation. *Acta Biomater.* **7**, 3515–3522 (2011).
40. Mostaed, E. et al. Novel Zn-based alloys for biodegradable stent applications: design, development and in vitro degradation. *J. Mech. Behav. Biomed. Mater.* **60**, 581–602 (2016).
41. Guo, P. et al. Ultrafine- and uniform-grained biodegradable Zn-0.5Mn alloy: Grain refinement mechanism, corrosion behavior, and biocompatibility in vivo, Materials Science and Engineering: C, 118 111391. (2021).
42. Wang, C., Yang, H. T., Li, X. & Zheng, Y. F. In vitro evaluation of the feasibility of commercial Zn alloys as biodegradable metals. *J. Mater. Sci. Technol.* **32**, 909–918 (2016).
43. Lévesque, J., Hermawan, H., Dubé, D. & Mantovani, D. Design of a pseudo-physiological test bench specific to the development of biodegradable metallic biomaterials. *Acta Biomater.* **4**, 284–295 (2008).
44. Xue, P. et al. Microstructure, mechanical properties, and in vitro corrosion behavior of biodegradable Zn-1Fe-xMg alloy. *Materials* **13**, 4835 (2020).

Acknowledgements

This work was conducted with fnancial support by the National Natural Science Foundation of China (Grant No. 42176209), and the Natural Science Foundation of Shandong Province (Grant No. ZR2021MD064).

Author contributions

Xin Cheng: Methodology, Formal analysis, Investigation, Writing - original draft, Writing – review & editing. Qiuju Lin: Visualization, Writing – review & editing. Hongxi Jin: Visualization, Writing – review & editing. Fufang Han: Methodology, Formal analysis, Investigation. Xiaohui Dou: Visualization, Writing – review & editing. Xinwei Zhang: Writing – review & editing. Zonghao He: Visualization, Writing – review & editing. Chuan

He: Visualization, Writing – review & editing. Songnan Zhao: Visualization, Writing – review & editing. Dalei Zhang: Supervision, Project administration, Funding acquisition.

Declarations

Competing interests
The authors declare no competing interests.

Additional information
Correspondence and requests for materials should be addressed to D.Z.

Reprints and permissions information is available at www.nature.com/reprints.

Publisher's note Springer Nature remains neutral with regard to jurisdictional claims in published maps and institutional affiliations.